Materials and Design 202 (2021) 109525

Contents lists available at ScienceDirect

Materials and Design

journal homepage: www.elsevier.com/locate/matdes

Substrate design to minimize residual stresses in Directed Energy Deposition AM processes

Xufei Lu [a,b,c], Michele Chiumenti [a,*], Miguel Cervera [a], Junjie Li [b,c], Xin Lin [b,c,**], Liang Ma [b,c], Guohao Zhang [b,c], Enquan Liang [d]

[a] International Center for Numerical Methods in Engineering, Universidad Politécnica de Cataluña, 08034 Barcelona, Spain
[b] State Key Laboratory of Solidification Processing, Northwestern Polytechnical University, Xi'an, Shaanxi 710072, China
[c] Key Laboratory of Metal High Performance Additive Manufacturing and Innovative Design, MIIT China, Northwestern Polytechnical University, Xi'an, Shaanxi 710072, China
[d] Shanghai Aircraft Design and Research Institute, Commercial Aircraft Corporation of China, Shanghai 200232, China

HIGHLIGHTS

- Substrate design optimization to reduce the residual stresses in DED.
- Coupled thermomechanical analysis for AM by an in-house calibrated software.
- Sensitivity of conformal and non-conformal substrates to the lower built surface.
- Sensitivity of substrate stiffness and thermal resistance on residual stresses.

GRAPHICAL ABSTRACT

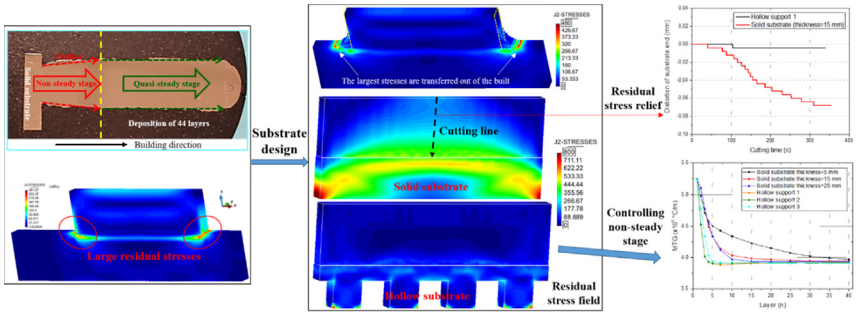

ARTICLE INFO

Article history:
Received 30 September 2020
Received in revised form 12 January 2021
Accepted 24 January 2021
Available online 28 January 2021

Keywords:
Directed energy deposition (DED)
Substrate design
Residual stresses
Thermo-mechanical analysis

ABSTRACT

This paper proposes a strategy to optimize the design of the substrate structures used in Additive Manufacturing (AM) by Directed Energy Deposition (DED) to minimize the residual stresses induced by this fabrication process. To this end, several numerical analyses were performed to analyse different substrate designs in order: (i) to reduce the sensitivity to the initial non-steady stage when the first layers of material are deposited, (ii) to optimize the heat flux through the substrate to reduce the Maximum Temperature Gradients (MTG) and, (iii) to modify the substrate stiffness and its mechanical constraining to the thermal deformations during the building process and the cooling phase. To ensure the reliability of the numerical simulations, an in-house software is calibrated to allow for an accurate analysis of DED. Thus, an experimental setting is undergone to feed the numerical model with suitable values of both material and process parameters through temperature and displacement measurements and numerical fitting. Once calibrated, the software is used to evaluate the performance of several substrate designs to mitigate the residual stresses induced by the DED process. A thin-walled rectangular part selected as industrial demonstrator showed a significant reduction (up to 62%) of the maximum tensile stresses.

1. Introduction

Additive manufacturing (AM) is an advanced industrial technology for manufacturing high-performance metallic parts through a layer-by-layer material deposition [1,2]. In Directed Energy Deposition (DED) the metal powder is blown into the melting pool generated by a coaxial high energy source (e.g. laser or electron beam). Despite

* Corresponding author.
** Corresponding author at: State Key Laboratory of Solidification Processing, Northwestern Polytechnical University, Xi'an, Shaanxi 710072, China.
E-mail addresses: michele.chiumenti@upc.edu (M. Chiumenti), xlin@nwpu.edu.cn (X. Lin).

https://doi.org/10.1016/j.matdes.2021.109525

being one of the most versatile AM processes used either to fabricate new components or to repair damaged parts [3], the DED technology is characterized by high-energy sources which generate high temperature fields as well as high temperature gradients. As a consequence, both residual (tensile) stresses and plastic deformations generally affect the final metallurgy as well as the structural performance of in service AM parts [3–5,38,39].

To mitigate the residual stresses and distortions of AM components, several researchers have investigated the sensitivity of the DED process to the scanning strategy, the process parameters and the geometry of the built structures. It has been observed that the residual stresses can be mitigated by reducing the local heat accumulation during the metal deposition. This can be achieved by reducing the scanning length and/or by increasing the scanning speed [6–8]. The substrate distortion can be alleviated by optimizing the process parameters (e.g. source power, scanning speed, feeding rate, etc.) [9–11]. Some other research works [12–15] revealed that the geometry of the component and, in particular, its local stiffness, also plays an important role in the development of residual stresses in the build. Mukherjee et al. [16,17] demonstrated how the thermal distortion of AM parts depends on the material properties, the deposition strategy, the process parameters, the geometry of the component, as well as the preheating and the cooling conditions. Mitigation of residual stresses can be achieved by preheating the substrate before the AM process, thus reducing of the large thermal gradients during the metal deposition of the first few layers [18–20]. Li et al. [21] reported a remarkable reduction of both longitudinal bending and angular distortion by replacing continuous clamping condition with a more flexible multi-point support strategy. Denlinger et al. [22] optimized the metal deposition on the base plate to mitigate the longitudinal bending effects induced by the thermal field. Afazov et al. [23,24] proposed the geometry compensation strategy to modify the nominal geometry of AM components according to the thermal deformation predicted by the numerical analysis. Finally, Hönnige et al. [25,26] showed the advantages of the rolling techniques in WAAM processes to reduce distortions and residual stresses.

Fig. 1 shows the transition from the "*non-steady stage*" to the "*quasi-steady stage*" during the DED process of a Ti-6Al-4V rectangular frame [12]. During the entire non-steady stage, both the thickness and the width of the deposited layers are affected by the heat absorption through the (initially) cold substrate. As a general conclusion, in DED process net-shape (nominal) geometries can obtained by reducing the Maximum Thermal Gradients (MTG). Such MTG generally appear when the first layers of metal are deposited on the cold substrate. Therefore, to enhance the DED process it is mandatory to reduce the MTG by either pre-heating the substrate [18–20] or reducing the heat flux from the Heat Affected Zone (HAZ) to the workbench through the substrate [6–9,25–28]. Thereby, the first objective of this work consists of optimizing the non-steady stage to obtain high quality DED parts.

In Selected Laser Melting (SLM) the workbench is very thick and rigid. Therefore, the focus is placed on the stiffness and the heat flux transfer of the support structures [29–31]; these are necessary when printing overhangs in SLM and they affect the development of thermal stresses and deformations of the build [29–33]. Contrariwise, in DED processes the material is directly deposited on the substrate and the use of supporting structure is generally avoided. Therefore, the overall stiffness of the building structure depends on the design of the substrate and its optimization is marginally studied in the literature. A thick substrate fixed on the work-bench is generally used to prevent the development of undesired thermal deformations. However, a very rigid substrate generates large residual stresses which can transform into plastic deformations during the cooling process. Moreover, during the cutting process when the substrate is removed, the residual stresses relaxation induces a further distortion of the component [17]. Thus, the optimization of the substrate stiffness in order to mitigate the residual stresses and the component distortion is the second objective of this work.

2. Numerical model

The numerical framework used for the high-fidelity modelling of AM processes is based on a coupled 3D thermo-mechanical FE module for transient analysis as part of the in-house software platform COMET [34] developed at the *International Centre for Numerical Methods in Engineering* (CIMNE). The thermo-mechanical coupling is handled by a staggered solution: at each time-step, the transient heat transfer problem is solved first. Next, the mechanical analysis is solved accounting for the temperature-dependent material parameter data-base.

2.1. Thermal analysis for AM

The balance of energy is the governing equation used to solve the heat transfer analysis. The local (strong) form of this equation is:

$$\dot{H} = -\nabla\cdot\mathbf{q} + + \dot{Q} \tag{1}$$

where $\dot{H}$ is the enthalpy rate. The heat flux $\mathbf{q}$ is defined through Fourier's law:

$$\mathbf{q} = -k\nabla T \tag{2}$$

where k is the temperature-dependent thermal conductivity.

The heat source (per unit of volume), $\dot{Q}$, is defined in terms of the total energy input (e.g. laser source), $\dot{P}$, the heat absorption efficiency, η_p and the volume of the melt pool, $V_{pool}^{\Delta t}$, as:

$$\dot{Q} = \frac{\eta_p \dot{P}}{V_{pool}^{\Delta t}} \tag{3}$$

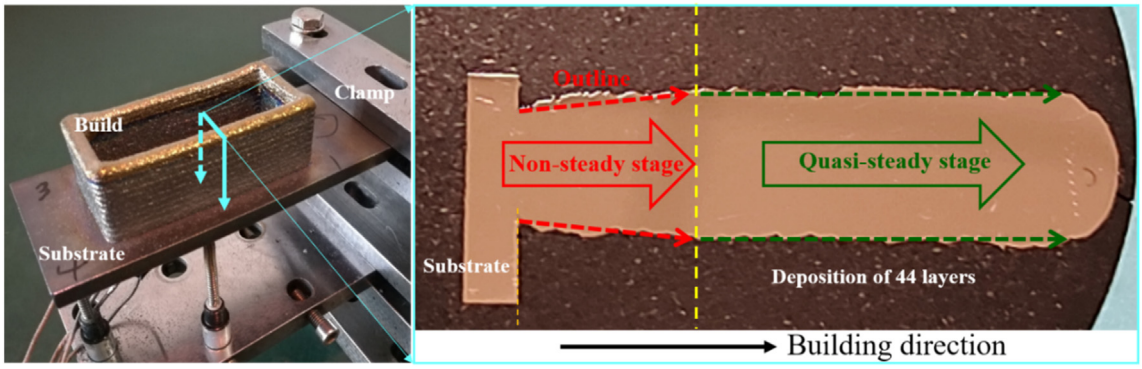

Fig. 1. The transition from the non-steady stage to quasi-steady stage of a Ti-6Al-4V part deposited by DED.

Hence, the heat source is uniformly spread inside the melt-pool because of the lack of resolution of the FE meshes generally used for the AM analysis at global (component) level [35–37].

The heat loss by convection is computed by using Newton's law:

$$q_{conv} = h_{conv}(T - T_{env}) \tag{4}$$

where h_{conv} is the temperature-dependent Heat Transfer Coefficient (HTC) by convection, T is the temperature at the component surface and T_{env} is the environment temperature.

The heat dissipation by the radiation is defined by Stefan-Boltzmann's law:

$$q_{rad} = \varepsilon_{rad}\sigma_{rad}\left(T^4 - T_{env}^4\right) \tag{5}$$

where ε_{rad} is the surface emissivity and σ_{rad} is the Stefan-Boltzmann constant.

Note that the heat dissipation by convection and radiation mechanism depends on the actual boundary condition (i.e. the current external surfaces of the built). Thus, the heat flow is proportional to the evolution of the building process [35–37].

2.2. Mechanical analysis

The mechanical problem is determined by the balance of momentum and the continuity equations:

$$\nabla\cdot\mathbf{s} + \nabla p + \mathbf{b} = 0 \tag{6}$$

$$(\nabla\cdot\mathbf{u} - e^T) - \frac{p}{K} = 0 \tag{7}$$

where the Cauchy stress tensor, $\boldsymbol{\sigma}$ is split into its hydrostatic (pressure), p and deviatoric parts $\mathbf{s}$, respectively, as:

$$\boldsymbol{\sigma} = p\boldsymbol{I} + \mathbf{s}(\mathbf{u}) \tag{8}$$

$\mathbf{b}$ are the body forces per unit of volume and $K(T)$ is the temperature-dependent bulk modulus, controlling the material compressibility. The thermal deformation, e^T is expressed as:

$$e^T(T, f_S) = e^{cool}(T) + e^{pc}(f_S) \tag{9}$$

$e^{cool}(T)$ and $e^{pc}(f_S)$ are the thermal expansion/contraction and thermal shrinkage during the liquid-to-solid phase-change, as a function of the initial temperature T_0 and the solid fraction f_S, respectively, and defined as:

$$e^{cool}(T) = \alpha(T)(T - T_0) \tag{10}$$

$$e^{pc}(f_S) = \beta f_S \tag{11}$$

where $\alpha = \alpha(T)$ and $\beta = \frac{\Delta V^{pc}}{V_0}$ are the thermal expansion and the shrinkage coefficients, respectively.

Note that the mechanical problem defined by Eqs. (6)–(7) depends on both the displacements, $\mathbf{u}$, and the pressure field, p and is suitable for both compressible and the fully incompressible (isochoric) material behaviors.

In AM, the temperature field varies from the room temperature to (and above) the melting point. Thereby, the material must be characterized in its solid, mushy and liquid phases.

A *J2*-thermo-elasto-visco-plastic model is assumed in the solid phase, from the room to the annealing temperature. All the material properties are assumed as temperature-dependent. The von-Mises yield-surface is defined as:

$$\Phi(\mathbf{s}, q_h, T) = \|\mathbf{s}\| - \sqrt{\frac{2}{3}}\left[\sigma_y(T) - q_h\right] \tag{12}$$

where $\sigma_y(T)$ is the temperature-dependent elastic limit controlling the thermal softening and q_h is the stress-like variable controlling the isotropic strain-hardening, expressed as:

$$q_h(\xi, T) = -\left[\sigma_\infty(T) - \sigma_y(T)\right]\left[1 - e^{-\delta(T)\xi}\right] - h(T)\xi \tag{13}$$

where ξ is the isotropic strain-hardening variable, $\sigma_\infty(T)$ is the temperature-dependent saturation flow stress, while $\delta(T)$ and $h(T)$ are the temperature-dependent parameters to control the exponential and linear hardening laws, respectively.

The deviatoric counterpart of Cauchy's stress tensor is computed as:

$$\mathbf{s} = 2G(\mathbf{e} - \mathbf{e}^{vp}) \tag{14}$$

where $G = G(T)$ is the temperature-dependent shear modulus, while $\mathbf{e}$ and $\mathbf{e}^{vp}$ are the total (deviatoric) and the visco-plastic strain, respectively. The former is extracted from the total strain tensor $\boldsymbol{\varepsilon}(\mathbf{u}) = \nabla^{sym}(\mathbf{u})$, while the evolution laws of both the visco-plastic strain tensor and the isotropic strain-hardening variable are obtained through the principle of maximum plastic dissipation as:

$$\dot{\mathbf{e}}\, vp = \dot{\gamma}\, vp \frac{\partial\Phi(\mathbf{s}, q_h)}{\partial\mathbf{s}} = \dot{\gamma}\, vp \frac{\mathbf{s}}{\|\mathbf{s}\|} = \dot{\gamma}\, vp\mathbf{n} \tag{15}$$

$$\dot{\xi} = \dot{\gamma}\, vp \frac{\partial\Phi(\mathbf{s}, q_h)}{\partial q_h} = \sqrt{\frac{2}{3}}\dot{\gamma}\, vp \tag{16}$$

where $\mathbf{n}$ is the normal of the yield surface, and $\dot{\gamma}\, vp$ is the visco-plastic multiplier, defined as:

$$\dot{\gamma}\, vp = \left\langle \frac{\partial\Phi(\mathbf{s}, q_h)}{\eta} \right\rangle^{\frac{1}{m}} \tag{17}$$

where $\langle\cdot\rangle$ is the Macaulay bracket, while $\eta = \eta(T)$ and $m = m(T)$ are the temperature-dependent plastic viscosity and rate sensitivity, respectively.

Note that, when the temperature is approaching the annealing value, $\sigma_y(T) \to 0$. Thus, the deviatoric Cauchy stress reduces to:

$$\mathbf{s} = \eta(\dot{\gamma}\, vp)^m\mathbf{n} = \eta_{eff}\dot{\mathbf{e}}\, vp \tag{18}$$

where $\eta_{eff} = \eta(\dot{\gamma}\, vp)^{m-1}$ is the effective viscosity. Thereby, above the annealing temperature the material is characterized by a purely viscous law [36,37]. A non-Newtonian behavior $m > 1$ is used for the mushy phase (from the annealing to the liquid temperature), while a Newtonian law, $m = 1$, characterizes the liquid phase (temperature values above the melting point).

2.3. FE modelling of the DED process

To simulate the DED process, a time discretization is required. A time step, $\Delta t = t^{n+1} - t^n$, characterizes the time-marching scheme. Thereby, the melt-pool is allowed to move step-by-step along the scanning pattern from the actual position defined at time t^n to that at time t^{n+1}. Within this interval, the heat is distributed to the elements belonging to the melt pool volume and, at the same time, the blown powder conforms the metal deposition which characterizes this AM process.

The numerical simulation of the DED process needs an ad-hoc procedure to classify the elements into: *active*, *inactive* and *activated* elements. At each time-step, an octree-based searching algorithm is used to find the elements belonging to the melt-pool (*active*) and to the new metal deposition (*activated*). Thus, the software reads the same input file (Common Layer Interface – CLI format) following the actual

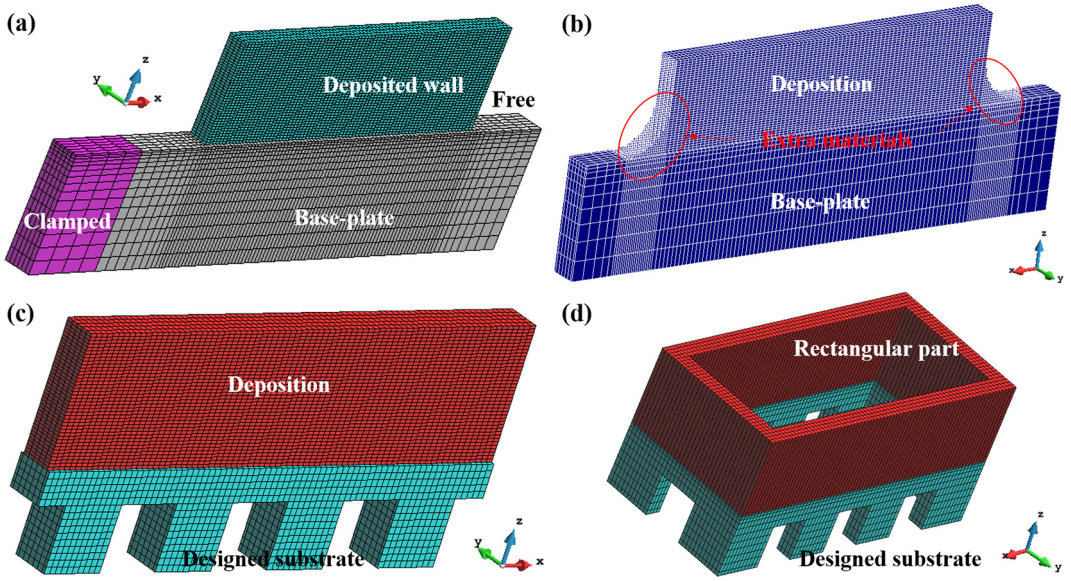

Fig. 2. 3D FE meshes used for analysing the DED process: (a) single-wall used to calibrate the AM model; (b) single-wall with rounded corners; (c) hollow structure design for the substrate; (d) demonstrator with hollowed structure substrate.

Table 1
Temperature-dependent material properties of Ti-6Al-4V [12].

Temperature (°C)	Density (kg/m^3)	Thermal Conductivity (W/(m·°C))	Heat Capacity (J/(kg·°C))	Poisson's Ratio	Thermal Expansion Coefficient (μm/(m·°C))	Young's Modulus (GPa)	Elastic Limit (MPa)
20	4420	7	546	0.345	8.78	110	850
205	4395	8.75	584	0.35	10	100	630
500	4350	12.6	651	0.37	11.2	76	470
995	4282	22.7	753	0.43	12.3	15	13
1100	4267	19.3	641	0.43	12.4	5	5
1200	4252	21	660	0.43	12.42	4	1
1600	4198	25.8	732	0.43	12.5	1	0.5
1650	3886	83.5	831	0.43	12.5	0.1	0.1
2000	3818	83.5	831	0.43	12.5	0.01	0.01

scanning sequence as used to inform the DED machine. The birth-and-death-element technique is used to activate the elements belonging to the new deposited layer. Both *active* and *activated* elements belong to the current computational domain, while the *inactive* elements are neither computed nor assembled into the global matrix of the problem [35].

2.4. Geometry model and FE meshes

The generation of the CAD geometry, the meshing operation as well as the post-processing of the results are carried out using the in-house pre-post-processor GiD [40]. Fig. 2 shows the 3D geometries and the corresponding FE meshes of different builds. Fig. 2(a) shows the single-wall model used to calibrate the AM software: it consists of 19,040 hexahedral elements and 24,285 nodes. The base plate is clamped on the left-hand side as a cantilever beam, while the other end is free. Fig. 2(b) shows the same geometry but including some extra material to alleviate the stress concentrations at the corners where the wall is attached to the substrate. Fig. 2(c) depicts a new substrate design characterized by a hollow structure, proposed to reduce the residual stresses and the sensitivity to the initial non-steady stage. Finally, a more complex part is presented in Fig. 2(d) and it is used as the industrial demonstrator to validate the optimization strategy for the substrate design. The corresponding mesh consists of 44,000 hexahedral elements and 56,400 nodes.

2.5. Material properties and boundary conditions

The temperature-dependent thermal and mechanical properties of Ti-6Al-4V adopted for the material characterization are listed in Table 1 [12]. Note that the thermal conductivity is increased up to 83.5 W/(m·°C) to take into account the convective flow inside the melting pool when the temperature is above the melt point [41].

The thermal boundary conditions adopted for all the numerical simulations account for the heat loss by convection and radiation through the external surfaces of both the build and the substrate. The HTC by convection and the emissivity are $h_{conv} = 8$ W/(m^2·°C) and $\varepsilon_{rad} = 0.7$, respectively. The HTC by conduction controlling the heat flux at the contact interface between the base-plate and the clamping system (or the workbench) is set to $h_{conv} = 100$ W/(m^2·°C). During the AM process, the ambient temperature was $T_{env} = 25$ °C. The power absorption in DED process when using Ti-6Al-4V is set to $\eta_p = 0.3$.

These parameters have been calibrated using the experimental data obtained through the in situ measurements as described in the next section.

3. Experimental setting

Fig. 3 shows the experimental setting used for the calibration of the software platform. The single-wall shown in Fig. 2(a) is used for this

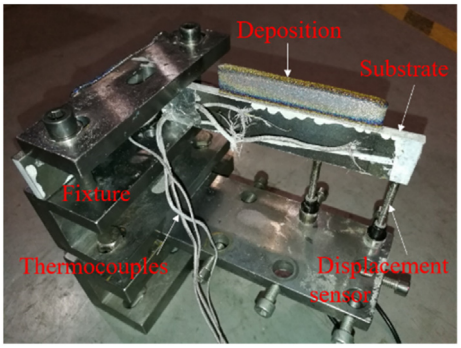

Fig. 3. In-situ measurement set-up for the calibration of the numerical simulation of the DED process: single-wall on a substrate fixed as a cantilever.

purpose. An annealed Ti-6Al-4V substrate 140 mm long, 6 mm wide and 25 mm high is used for the DED process.

Fig. 4 shows the locations of the thermocouples and the displacement sensor. The displacement sensor (WXXY PM11-R1-20L) has an accuracy of 0.02%, a maximum range of 20 mm and was employed for the in-situ measurement of the vertical displacement at point DS placed on the bottom surface of the substrate during the entire DED process. Omega GG-K-30 type thermocouples with a recording uncertainty of ±0.75% (or 2.2 °C) were used to measure the temperature history at points CH1, CH2, and CH3 of the substrate. Additionally, a Graphtec GL-900 high-speed eight-channel data-logger was used to record the signals from the thermocouples and displacement sensors.

Spherical Ti-6Al-4V powder (45–325 μm) produced via a plasma rotating electrode process is dried in a vacuum oven at 120 °C during 2.5 h before the blown-powder process. The DED machine is equipped with a YLS-3000 IPG Photonics fibre laser system having a wave-length ranging between 960 and 1200 nm and a maximum output power of 3 kW. During the fabrication, the laser power used was 1.5 kW with 3 mm of spot size and a Gaussian distribution profile. The laser scanning speed is 10 mm/s. The up-lift height is set to 0.5 mm with a feeding rate of 12.0 g/min. The average penetration depth is 0.5 mm.

The metal deposition is made of 40 layers, approximately 20 mm high, 80 mm long and 4 mm wide (one single hatching). The whole building process is carried out in a closed chamber with protective gas (pure argon).

4. Calibration of DED model

The thermo-mechanical FE model as well as the material data used in this work have been validated in previous works [3,12,19,35–37]. Here, only the heat dissipation by convection and conduction are calibrated. The numerical fitting of the experimental measurements is

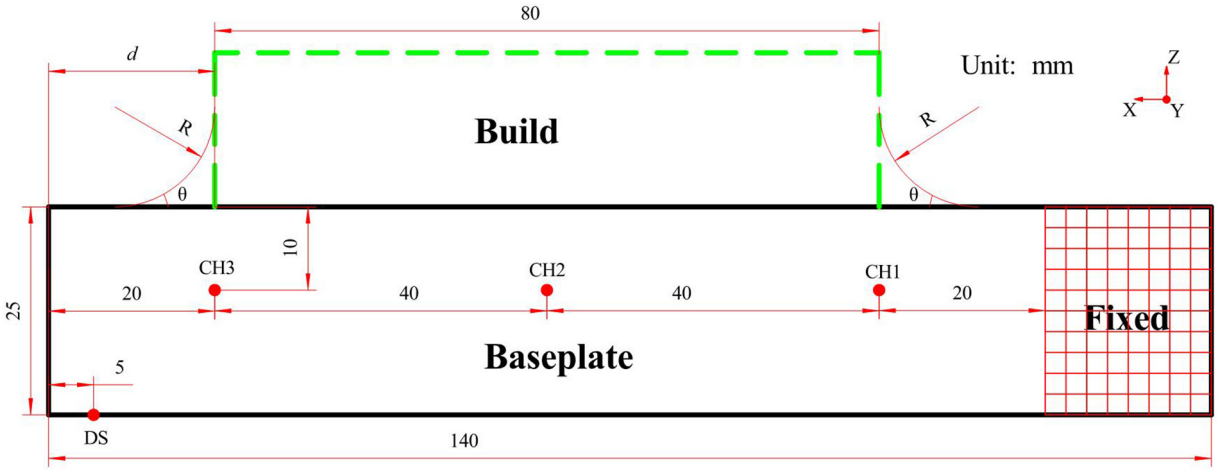

Fig. 4. Single-wall: dimensions and location of the thermocouples (CH1, CH2 and CH3) and the displacement sensor (DS).

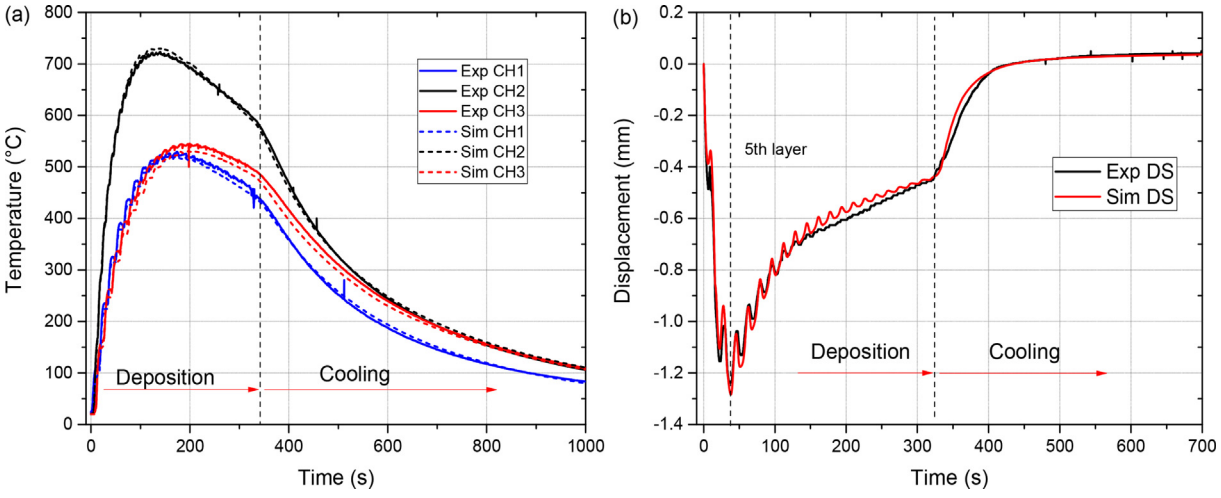

Fig. 5. Experimental measurements and numerical results: (a) temperature evolution at CH1, CH2 and CH3; (b) vertical displacement history at DS point.

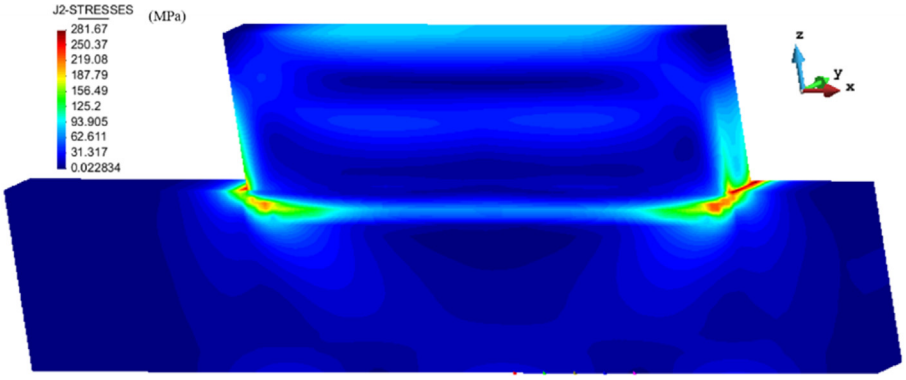

Fig. 6. Residual von Mises stress field of the single-wall.

shown in Fig. 5. In this figure, the temperature curves shown corresponds to the measurements at the thermocouple locations CH1, CH2 and CH3, while the vertical displacement is obtained at point DS (see Fig. 4). The agreement between experiments and numerical results is remarkable.

5. Substrate optimization strategy

Fig. 6 shows the von Mises stress indicator corresponding to the residual stress field at the end of the DED process. The highest values are located at the basement of the single-wall deposition, as previously observed in [3,12,17]. This is mainly due to the large temperature gradients generated during the deposition of the first layers of the building over the cold substrate during the initial non-steady stage. The contraction of these layers is restrained by the substrate, thus generating large residual stresses.

The optimization of the substrate geometry aims both to enhance the heat dissipation through the substrate and to reduce its global stiffness. On the one hand, if the heat flux is reduced, the thermal gradients during the initial non-steady stage of the metal deposition can be reduced also. On the other hand, by reducing the global stiffness of the substrate, it is possible to achieve a weaker mechanical constraining between the AM-build and the substrate, reducing the formation of plastic deformations. The drawback of the latter is the possibility of inducing a larger distortion of the component.

5.1. Minimization of the stress concentrations

In order to minimize the stress concentrations at the interface between the building structure and the substrate, two possibilities are investigated: (i) rounding off the sharp angles where the part is attached to the substrate; and (ii) conforming the substrate to the bottom surface of the build.

The first idea is very well known and is actually applied in many fabrication processes to avoid crack initiation at the stress concentration points. Therefore, all the corners are rounded off to avoid sharp angles.

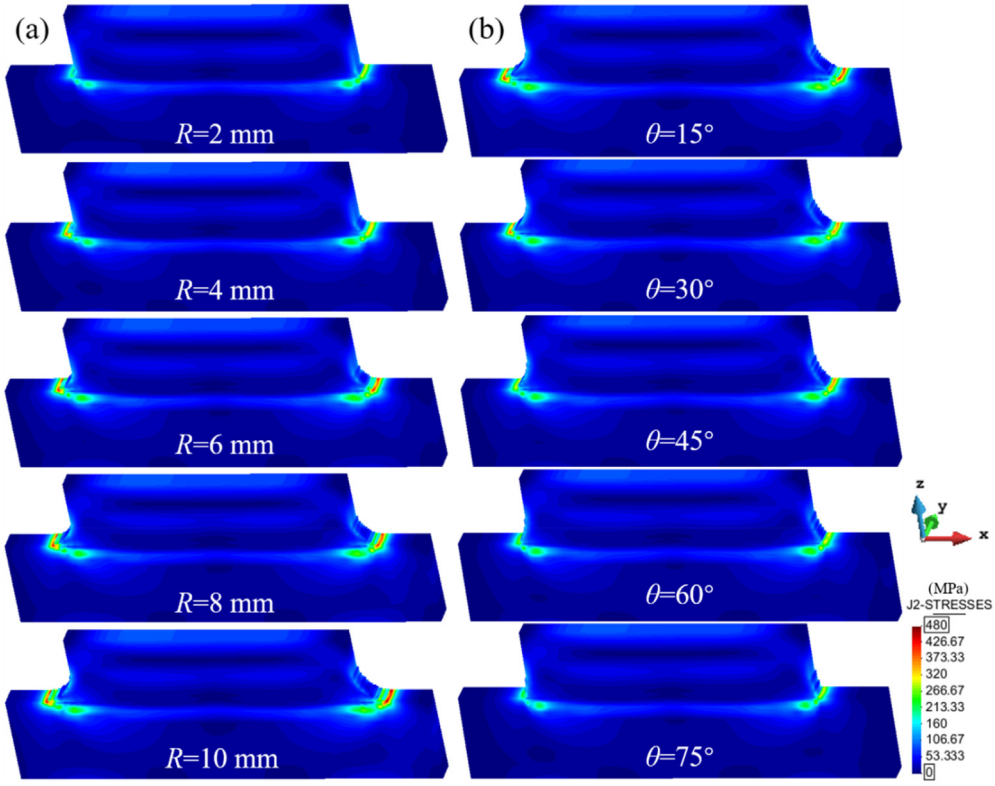

Fig. 7. Predicted residual von Mises stress field: (a) by rounding off the corners using different arc radii (R). (b) by using different tangent angles (θ) with respect to the substrate.

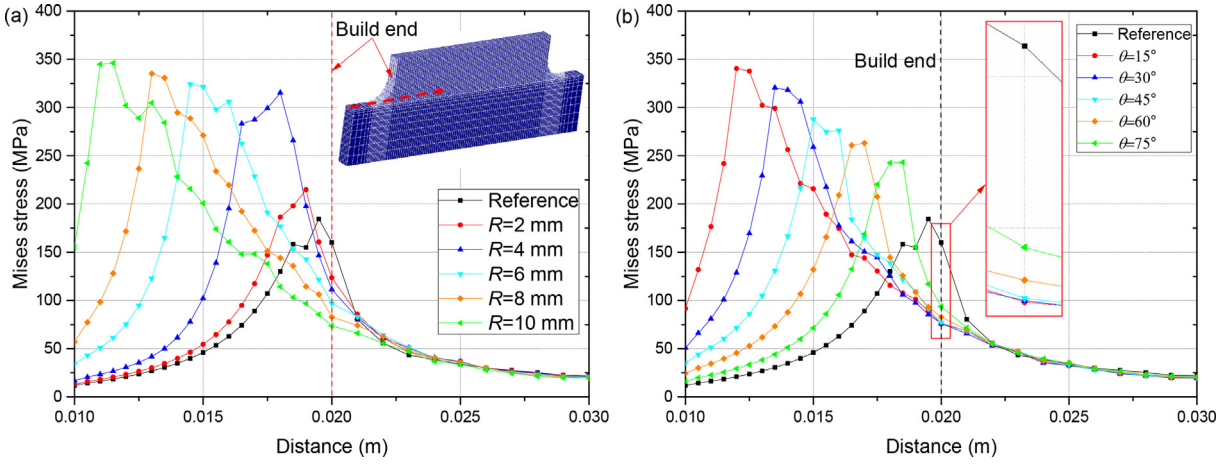

Fig. 8. Comparison of the residual von Mises stress distributions along the top surface of the substrate: (a) by rounding off the corners using different arc radii (R); (b) by using different tangent angles (θ) with respect to the substrate.

The effectiveness of this method in AM is tested in this work by taking the rounding angle θ between top surface of the substrate and the single-wall as the design parameter. The sample with sharp angles is used as the reference.

Figs. 7(a) and 8(a) show the contour fills and the distributions of the residual von Mises stress using different rounding radii varying from 2 to 10 mm. In both figures, it can be observed that the maximum residual stresses increase by expanding the arc radius. This is due to the fast cooling of the extra material used to print this small zone. However, the highest stress values are located outside the nominal geometry of the single-wall, and more precisely, at the external sides of the material used for the rounding off. Thus, the residual stresses are effectively minimized in the actual build.

As an alternative, the material supply for the rounding off can be reduced assuming non-tangent configurations where the angle θ with respect to the substrate is varied from 15° to 75°. Also in this case, the values of the residual von Mises stress depicted in Fig. 7(b) and Fig. 8(b) are increasing when reducing θ but, again, the corresponding highest values are moved far away from the nominal geometry of the wall. Taking into account the material waste and practical experience, it is found that $\theta = 45°$ is the optimal choice for minimizing the stress concentration and preventing crack initiation.

5.2. Size optimization of the substrate

In this section, the optimization of the substrate size is investigated. The distance, d, between the left-hand side of the substrate and the single-wall is used as design parameter (see Fig. 4). This dimension is progressively reduced from 20 mm to 15 mm, 10 mm, 5 mm and 0 mm, respectively.

The evolution of the vertical displacement recorded during the entire DED process simulation is shown in Fig. 9(a) for all the test-cases. As the wall of the AM deposition gets closer to the free-end of the substrate, the vertical displacement of the substrate at point DS gradually decreases. It is also relevant to observe that most of the substrate distortion occurs during the non-steady stage, when the first 5 layers are deposited on the cold substrate. If compared with the reference configuration ($d =$ 20 mm), when $d = 0$ mm (i.e. the substrate conforms to the lower surface of the build), this vertical displacement is reduced by 30%. The longitudinal residual stress (σ_{xx}) distributions at the basement of the build are plotted in Fig. 9(b) and in the contour-fills shown in Fig. 10. It can be seen that the stress concentration on the right-hand side of the single-wall gradually decreases according to the size of the substrate, to vanish when $d = 0$. This is because the mechanical constraining induced by the substrate is gradually reduced, allowing for the free thermal

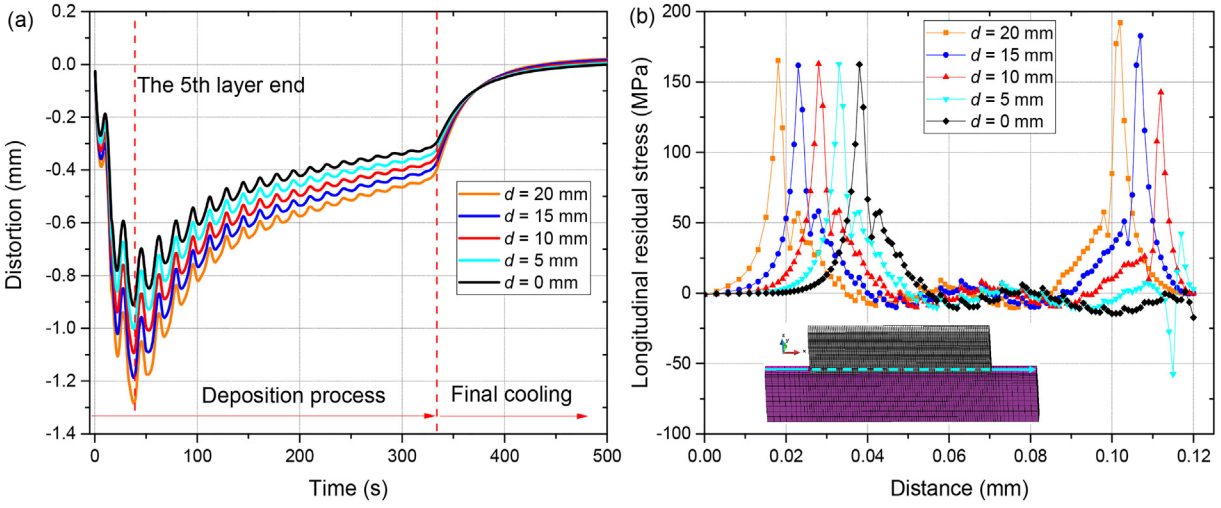

Fig. 9. Optimization of the substrate size for the single-wall: (a) vertical displacement histories at point DS; (b) distribution of longitudinal residual stresses (σ_{xx}) on the top surface of the substrate.

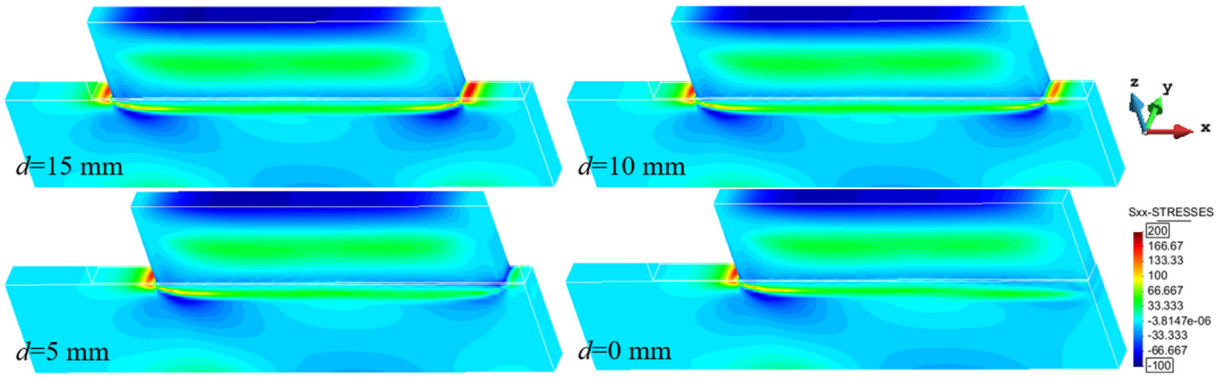

Fig. 10. Contour-fill of the longitudinal residual stress (σ_{xx}).

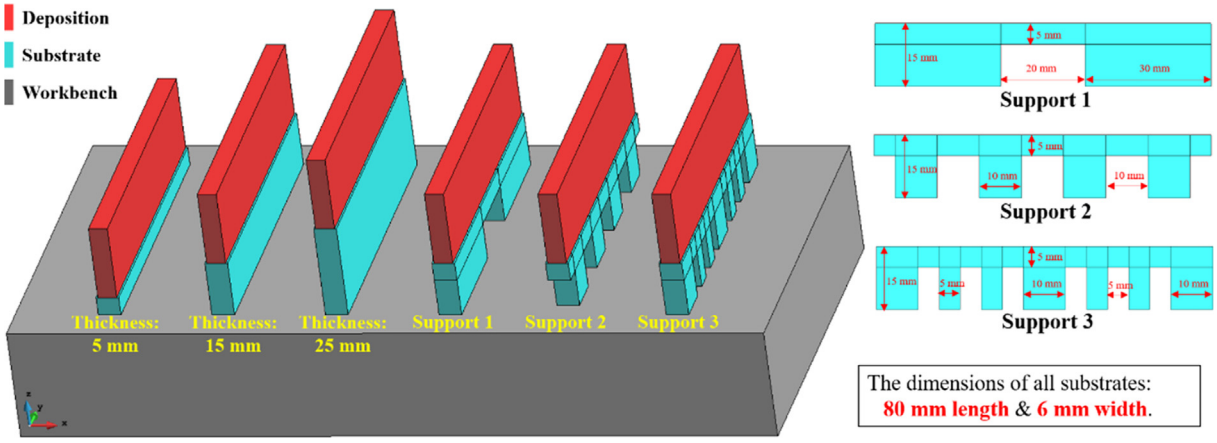

Fig. 11. Different substrates for the metal deposition part during DED process.

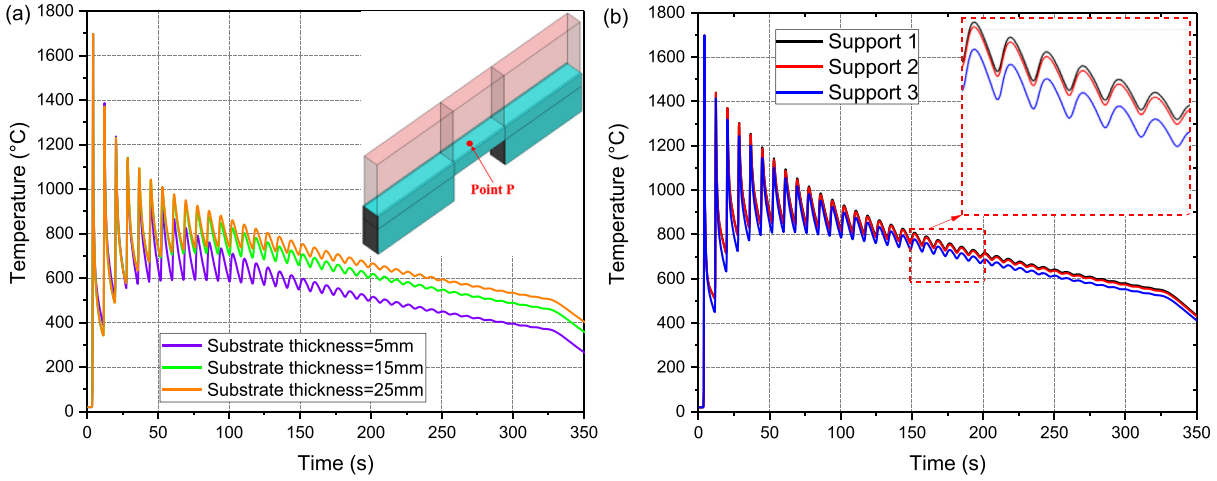

Fig. 12. Temperature evolution of point P: (a) solid substrates with increasing height; (b) hollow substrates.

expansion/contraction of the deposited materials. Thus, residual stresses during the AM process can be satisfactorily mitigated.

5.3. Optimization of the substrate design

In this section, the design optimization of the substrate structure is investigated. Two types of substrates are analyzed: (i) solid substrates with increasing height of 5 mm, 15 mm, and 25 mm, respectively; and (ii) hollow substrates with a fixed height of 15 mm but with different hollow shapes, as shown in Fig. 11. These structures are suitable for industrial DED fabrications and respond to two objectives: (1) reducing the heat flux through the substrate, and (2) reducing the substrate stiffness. As a consequence, the initial non-steady phase can be minimized because of a faster substrate heating. Moreover, the mechanical constraining due to the substrate stiffness is also reduced and thus, the residual stresses induced by the metal deposition process are mitigated.

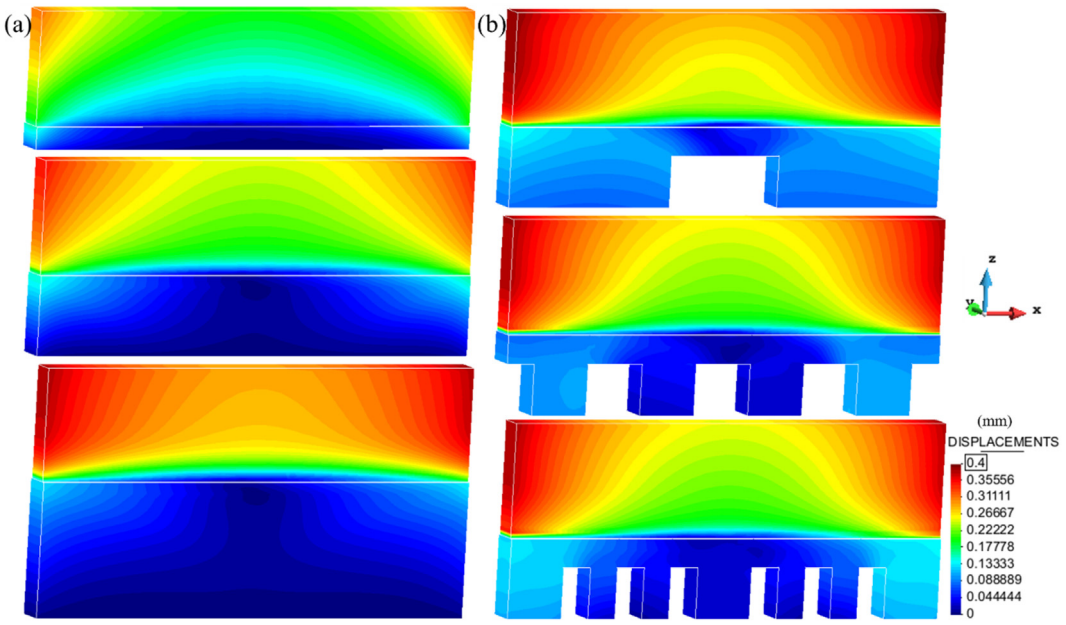

Fig. 13. Norm of the displacements of the single-wall according to the different substrates analyzed: (a) solid substrates; (b) hollow substrates.

The workbench is assumed as rigid, so the displacements at the bottom surface of the substrate are fixed as in the actual DED process. Moreover, the size of the substrate is reduced to 80 mm, the same as the single-wall. Therefore, the stress concentrations at both side of the single wall are avoided.

Fig. 12 shows the temperature evolution in the middle point of the top surface of the substrate for the three substrate thicknesses and for the three different hollow substrates. On the one hand, the higher is the substrate, the slower is the heat dissipation from the HAZ to the workbench through the substrate. Hence, the steady state conditions can be reached faster. On the other hand, the average temperature when using the hollow substrates is higher than in the cases of solid substrates. Therefore, the proposed design is helpful to increase the substrate temperature and to reduce the non-steady phase at the beginning of the DED process.

Fig. 13 shows the norm of the displacement field at the end of the DED process, for all the tested substrate structures. As shown in Fig. 13(a), by increasing the height of the solid substrate, the angular distortion of the build is also incremented. Thus, the hot material deposited during the fabrication of the single-wall is no longer able to contract because of the higher constraining of the substrate. However, the increased stiffness reduces the formation of residual stresses, as shown in Fig. 14(a).

A different behavior is appreciated when using the proposed hollow structures. In this case, the distortion is reduced by increasing the number of hollows without compromising the residual stress distribution as shown in Figs. 13(b) and 14(b), respectively.

Fig. 15 shows the predicted residual stresses at the interface between the single-wall and the substrate, for all the analyzed substrates.

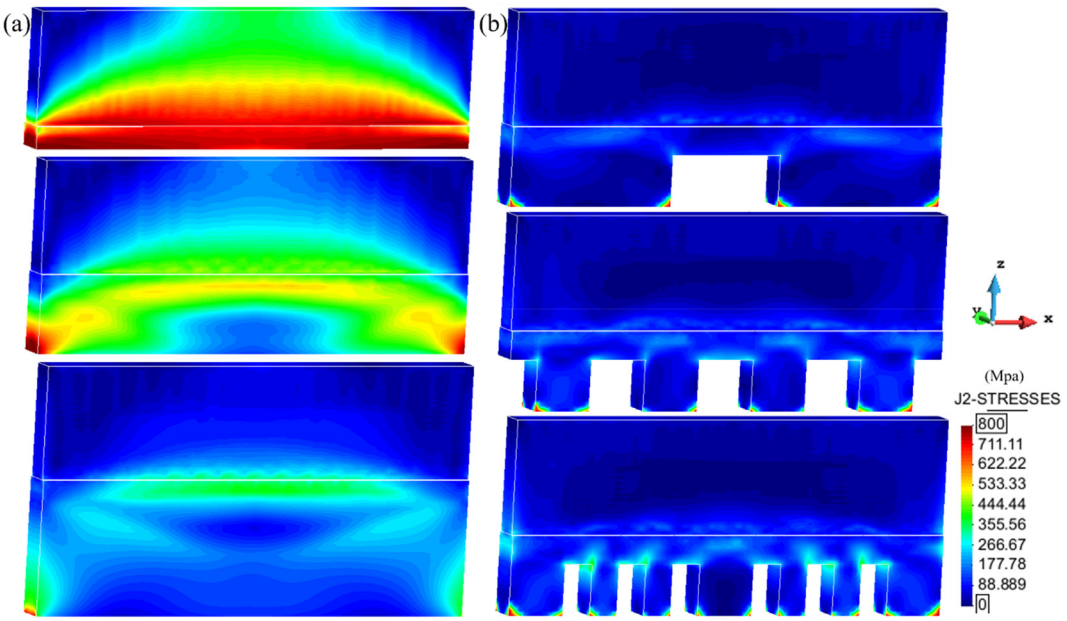

Fig. 14. Von Mises residual stress field at the end of the DED process: (a) solid substrates; (b) hollow substrates.

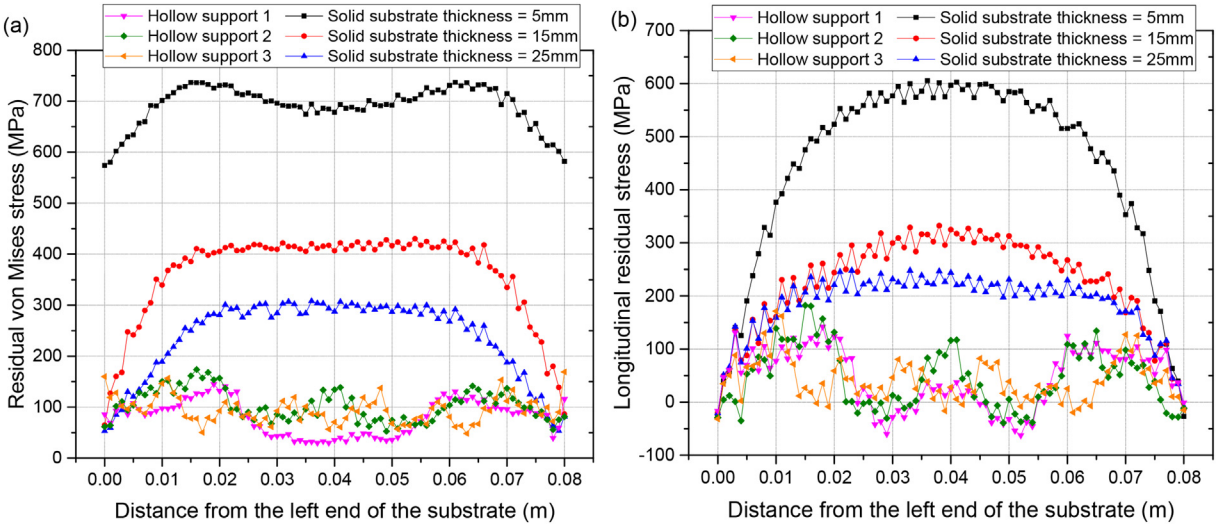

Fig. 15. Residual stress distributions on the wall-substrate interface for the different substrate structures: (a) von Mises stresses; (b) longitudinal stresses.

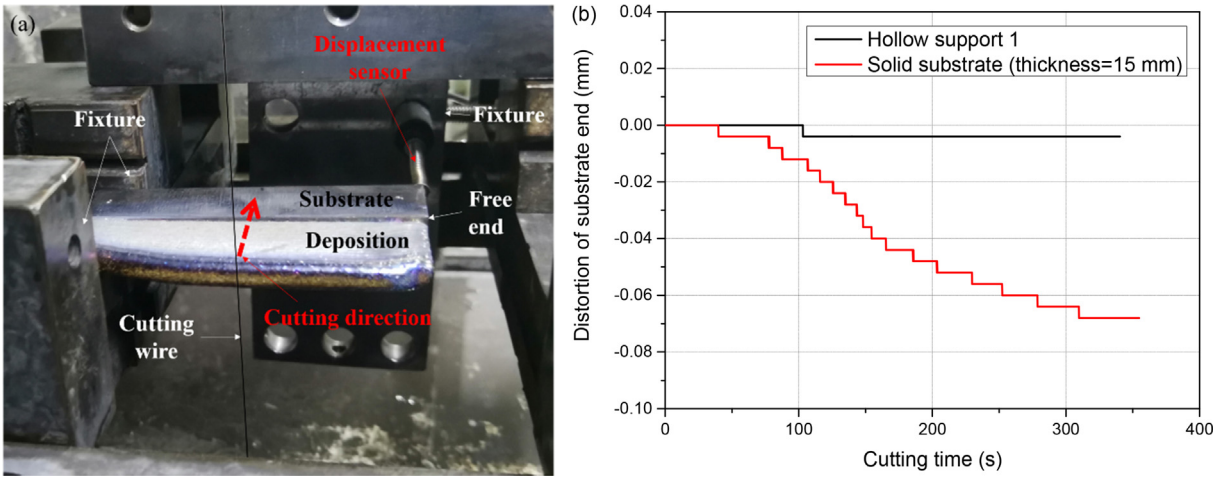

Fig. 16. Wire-cutting process: (a) cutting process; (b) evolution of the vertical displacement at the free end of the substrates as a function of the cutting time.

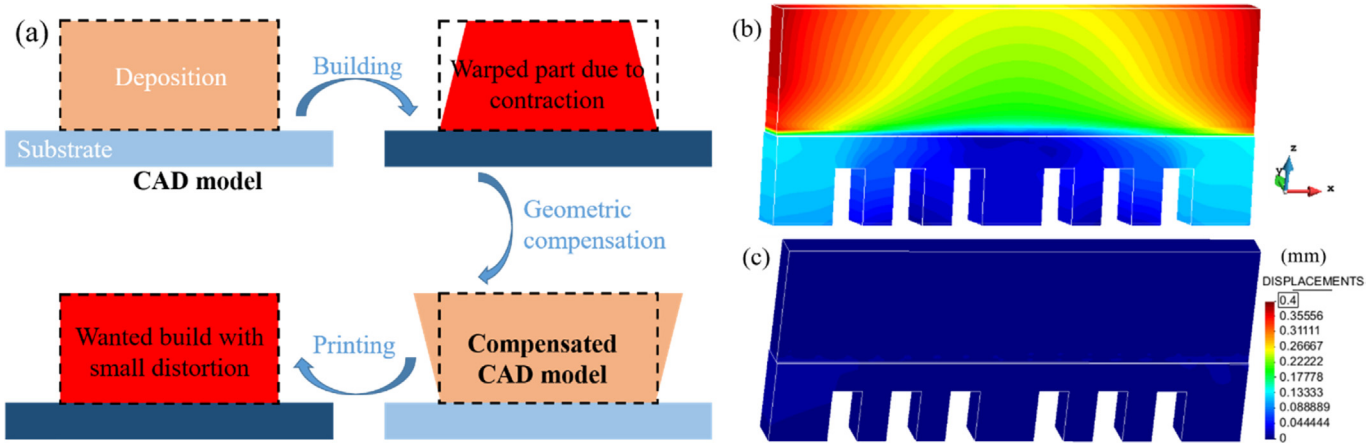

Fig. 17. Geometry compensation strategy: (a) required steps for the geometric compensation; (b) single-wall AM analysis without geometric compensation; (c) with geometric compensation.

Both longitudinal and von Mises stresses are mitigated when adopting hollow substrates.

To prove the effective mitigation of the residual stresses, both solid and hollow substrates are removed by wire-cutting, as shown in Fig. 16(a). The evolution of the vertical displacement at the free end of the part is presented in Fig. 16(b) as a function of the cutting time. It can be observed that the stress release induced by the cutting process of the solid substrate generates a pronounced residual distortion of the AM part. Contrarily, removing the hollow substrate only affects marginally the distortion of the single-wall. Therefore, the amount of residual stresses accumulated in the AM part when using the solid substrate is larger than for the hollow substrate.

As shown in Fig. 13, the drawback when reducing the substrate stiffness is the increase of thermal warpage. A possible solution to recover the nominal geometry is using the geometry compensation technique [23,24,42]. Fig. 17(a) summarizes the necessary steps: (1) starting from the nominal geometry, the DED process is simulated to compute the warpage due to the thermal deformation and material shrinkage; (2) this information is used to modify the nominal geometry generating the compensated model; (3) the process simulation is repeated to check if the resulting distortions do not exceed the fabrication tolerances. If this is not the case, steps (2) and (3) are repeated until the desired geometrical accuracy is reached. Fig. 17(b) illustrates the residual part distortion without geometry compensation, at the end of step (1), and at the end of the compensation loop (see Fig. 17(c)). Hence, this strategy can be efficiently used to obtain high precision AM components [42].

6. Validation of the substrate design strategy

The validation of the proposed methodology to improve the AM fabrication by DED is carried out using the rectangular-shape geometry shown in Fig. 18(a), used as demonstrator. The AM thermo-mechanical analysis of this component was reported in a previous work [12]. Here, the objective is to investigate three new substrate designs referred to as: solid, rectangular and hollow substrates, respectively. Also in this case, the workbench is not simulated and the bottom surface of all substrates is fixed.

The temperature evolution at point T for all substrates is depicted in Fig. 18(b), while the corresponding MTG (G_{xx}) along the scanning direction are shown in Fig. 18(c). As for the single-wall, reducing the mass of the substrate or/and defining a hollow structure induces higher peak and average temperatures of the substrate. Hence, the substrate is forced to heat faster reducing the transient stage. Also in this case, the hollow substrate shows the fastest fall of the MTG (Fig. 18 (c)), indicating the rapid establishment of the quasi-steady stage and a better performance being the preferred design for its industrialization.

Fig. 19 compares the evolution of the longitudinal stress (σ_{xx}) at the mid-point of the YZ cross-section for all the proposed substrate structures. This figure shows that, also in this case, the maximum longitudinal tensile stresses are produced at the interface between the part and the substrate just after the deposition of the first layer. By increasing the number of layers, the tensile stresses gradually reduce according to the reduction of the MTG (see Fig. 18(c)). Nevertheless, more flexible substrates produce lower tensile stresses in the build. The hollow substrate showed a 62% reduction of the maximum longitudinal tensile stress. Fig. 20 shows both the final distortion of the part (displacements norm) and the residual von Mises stress indicator for the different substrates analyzed. Also for the selected demonstrator, more flexible substrates generate lower residual stresses even if the final distortion can be slightly higher.

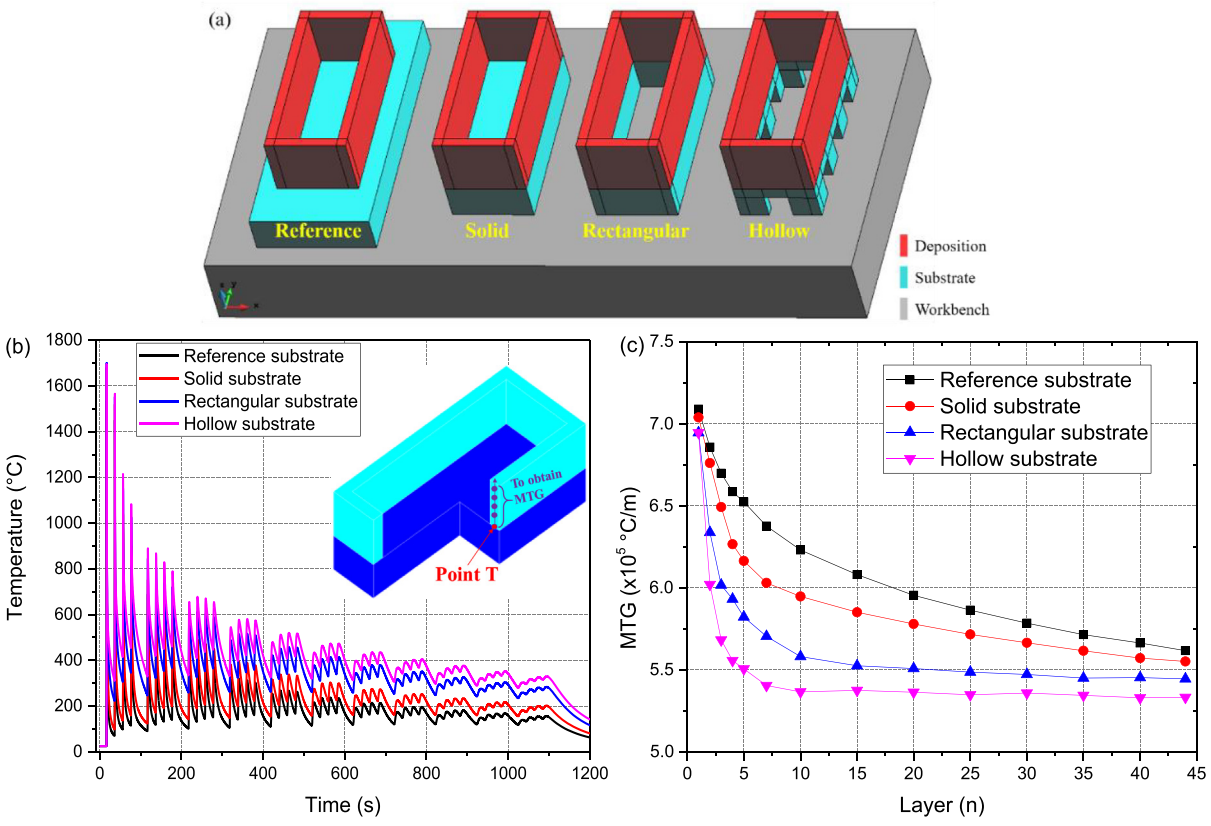

Fig. 18. Substrate structure optimization: (a) CAD geometries of the different substrates analyzed; (b) thermal histories at point T; (c) MTG (G_{xx}) evolution as a function of the number of deposited layers.

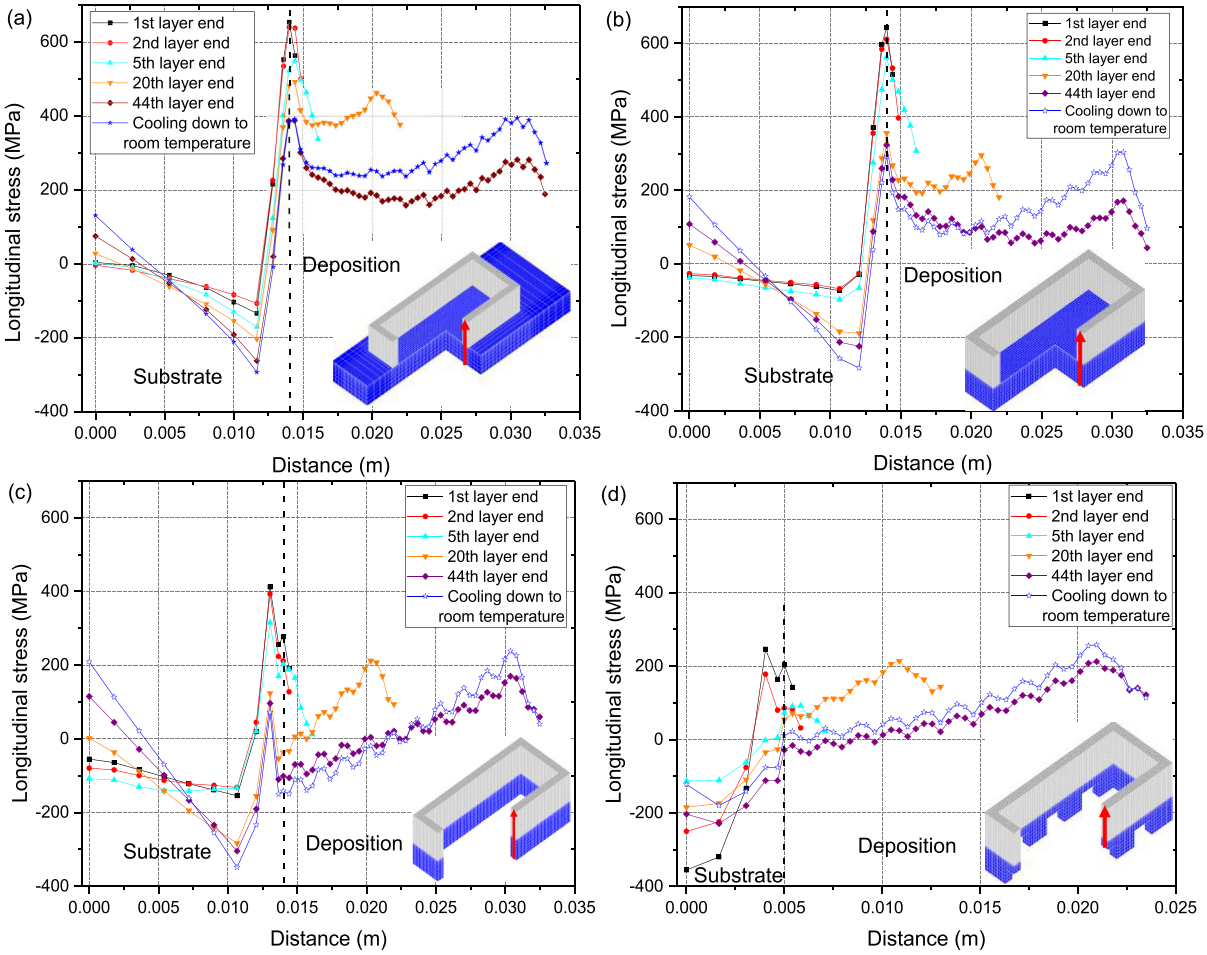

Fig. 19. Evolution of the longitudinal stresses (σ_{xx}) at the mid YZ cross section during the AM process: (a) reference substrate; (b) solid substrate; (c) rectangular substrate; (d) hollow substrate.

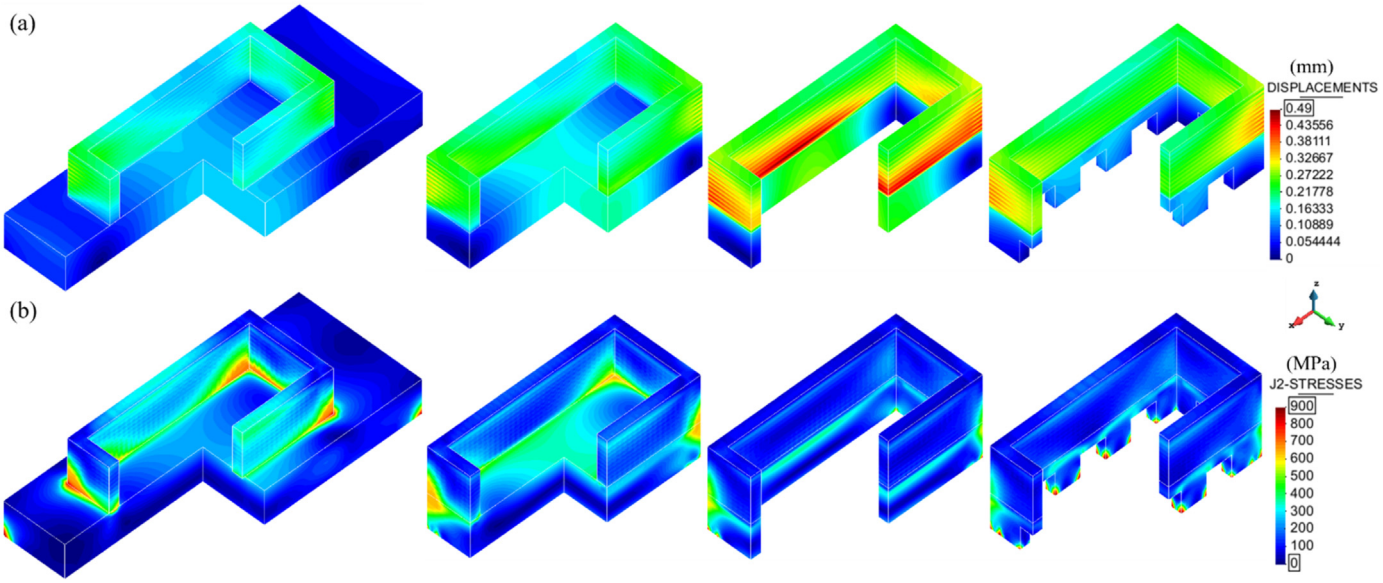

Fig. 20. Mechanical responses of the demonstrator: (a) final distortions (displacements norm); (b) residual von Mises stresses.

7. Concluding remarks

A 3D thermo-mechanical FE model is calibrated by in-situ experimental measurements using the single-wall structure fabricated by DED processes. This done, the software platform is used to analyse different substrate structures and some fabrication recommendations are drawn:

(1) Most of the residual stresses in DED processes are generated during the deposition of the first layers, when the substrate is still cold and very high temperature gradients develop. When the quasi-steady conditions are reached, much lower residual stresses are generated during the metal deposition.
(2) Rounding off sharp angles is a good practice to reduce the stress concentrations in AM as observed in many other fabrication processes. Moreover, focussing on the size of the substrate, the best option is to consider a substrate conformal to the bottom surface of the AM component, so that possible sharp angles are avoided and the flexibility of the substrate is enhanced.
(3) Reducing the size of the substrate is beneficial to mitigate residual stresses because both the heat flux and the stiffness are reduced, allowing for a faster non-steady stage and a lower mechanical constraining.
(4) Reducing the stiffness of the substrate can increase the final distortion and warpage of the AM-build. The geometric compensation strategy can be employed to recover the nominal geometry at the end of the fabrication.
(5) Hollow substrate structures reduce the transient stage of the DED fabrication. The heat flow through the substrate to the workbench is slowed. Hence, the substrate heats up much faster than in the case of a solid structures.

Declaration of Competing Interest

The authors declare no conflict of interest.

Acknowledgements

This research was funded by the National Key Technologies R & D Program (No. 2016YFB1100104) and the Natural Science Foundation of Shaanxi Province of China (Grant No. 2018JM5115). Funding from the Spanish Ministry of Economy and Competitivity (MINECO) under the ADaMANT project: Computational Framework for Additive Manufacturing of Titanium Alloy Components (ref: DPI2017-85998-P), within the Excellency Programme for Knowledge Generation is gratefully acknowledged. CIMNE is recipient of the Severo Ochoa Award of Excellence from MINECO. This work was also funded by the European KYKLOS 4.0 project: An Advanced *Circular and Agile Manufacturing Ecosystem based on rapid reconfigurable manufacturing process and individualized consumer preferences* (No. H2020-DT-2019-1).

References

[1] D. Herzog, V. Seyda, E. Wycisk, et al., Additive manufacturing of metals[J], Acta Mater. 117 (2016) 371–392.
[2] H. Huang, N. Ma, J. Chen, et al., Toward large-scale simulation of residual stress and distortion in wire and arc additive manufacturing[J], Add. Manufact. 34 (2020) 101248.
[3] X. Lu, X. Lin, M. Chiumenti, et al., In situ measurements and Thermo-mechanical simulation of Ti-6Al-4V laser solid forming processes[J], Int. J. Mech. Sci. 153 (2019) 119–130.
[4] Q. Wang, J. Shi, L. Zhang, et al., Impacts of laser cladding residual stress and material properties of functionally graded layers on titanium alloy sheet[J], Add. Manufact. 35 (2020) 101303.
[5] J.M. Shi, N. Ma, L.X. Zhang, et al., Residual stress and fracture strength of brazed joint of ceramic and titanium alloy with the aid of laser deposited functionally graded material layers[J], J. Manuf. Process. 34 (2018) 495–502.
[6] W. Woo, D.K. Kim, E.J. Kingston, et al., Effect of interlayers and scanning strategies on through-thickness residual stress distributions in additive manufactured ferritic-austenitic steel structure[J], Mater. Sci. Eng. A 744 (2019) 618–629.
[7] K. Ren, Y. Chew, J.Y.H. Fuh, et al., Thermo-mechanical analyses for optimized path planning in laser aided additive manufacturing processes[J], Mater. Des. 162 (2018) 80–93.
[8] Q. Wu, T. Mukherjee, C. Liu, et al., Residual stresses and distortion in the patterned printing of titanium and nickel alloys[J], Add. Manufact. 29 (2019) 100808.
[9] Y. Lee, Y. Bandari, P. Nandwana, et al., Effect of interlayer cooling time, constraint and tool path strategy on deformation of large components made by laser metal deposition with wire[J], Appl. Sci. 9 (23) (2019) 5115.
[10] F. Soffel, D. Eisenbarth, K. Wegener, Minimizing Substrate Distortion in Direct Metal Deposition (DMD) with Optimized Process Parameters and Buildup Strategies[C]// 3rd International Symposium on Additive Manufacturing (ISAM 2019), 2019.
[11] Z. Wang, E. Denlinger, P. Michaleris, et al., Residual stress mapping in Inconel 625 fabricated through additive manufacturing: method for neutron diffraction measurements to validate thermomechanical model predictions[J], Mater. Des. 113 (2017) 169–177.
[12] X. Lu, X. Lin, M. Chiumenti, et al., Residual stress and distortion of rectangular and S-shaped Ti-6Al-4V parts by directed energy deposition: modelling and experimental calibration[J], Add. Manufact. 26 (2019) 166–179.
[13] Q. Yang, P. Zhang, L. Cheng, et al., Finite element modeling and validation of thermomechanical behavior of Ti-6Al-4V in directed energy deposition additive manufacturing[J], Add. Manufact. 12 (2016) 169–177.
[14] A. Grégoire, L. Jakabčin, Taking into account thermal residual stresses in topology optimization of structures built by additive manufacturing[J], Math. Models Methods Appl. Sci. 28 (12) (2018) 2313–2366.
[15] R. Ranjan, Y. Yang, C. Ayas, et al., Controlling local overheating in topology optimization for additive manufacturing[C], Dimensional Accuracy and Surface Finish in Additive Manufacturing, 2017.
[16] T. Mukherjee, V. Manvatkar, A. De, et al., Mitigation of thermal distortion during additive manufacturing[J], Scr. Mater. 127 (2017) 79–83.
[17] H.L. Wei, T. Mukherjee, W. Zhang, et al., Mechanistic models for additive manufacturing of metallic components[J], Prog. Mater. Sci. 100703 (2020).
[18] J. Cao, M.A. Gharghouri, P. Nash, Finite-element analysis and experimental validation of thermal residual stress and distortion in electron beam additive manufactured Ti-6Al-4V build plates[J], J. Mater. Process. Technol. 237 (2016) 409–419.
[19] D.J. Corbin, A.R. Nassar, E.W. Reutzel, et al., Effect of substrate thickness and preheating on the distortion of laser deposited Ti–6Al–4V[J], J. Manuf. Sci. Eng. 140 (6) (2018), 061009.
[20] X. Lu, X. Lin, M. Chiumenti, et al., Finite element analysis and experimental validation of the thermomechanical behavior in laser solid forming of Ti-6Al-4V[J], Add. Manufact. 21 (2018) 30–40.
[21] F. Li, S. Chen, J. Shi, et al., In-process control of distortion in wire and arc additive manufacturing based on a flexible multi-point support fixture[J], Sci. Technol. Weld. Join. 24 (1) (2019) 36–42.
[22] E.R. Denlinger, P. Michaleris, Mitigation of distortion in large additive manufacturing parts[J], Proc. Inst. Mech. Eng. B J. Eng. Manuf. 231 (6) (2017) 983–993.
[23] S. Afazov, A. Okioga, A. Holloway, et al., A methodology for precision additive manufacturing through compensation[J], Precis. Eng. 50 (2017) 269–274.
[24] A. Yaghi, S. Ayvar-Soberanis, S. Moturu, et al., Design against distortion for additive manufacturing[J], Add. Manufact. 27 (2019) 224–235.
[25] J.R. Hönnige, P.A. Colegrove, B. Ahmad, et al., Residual stress and texture control in Ti-6Al-4V wire + arc additively manufactured intersections by stress relief and rolling[J], Mater. Des. 150 (2018) 193–205.
[26] J.R. Hönnige, P.A. Colegrove, S. Ganguly, et al., Control of residual stress and distortion in aluminium wire + arc additive manufacture with rolling[J], Add. Manufact. 22 (2018) 775–783.
[27] C. Baykasoğlu, O. Akyildiz, M. Tunay, et al., A process-microstructure finite element simulation framework for predicting phase transformations and microhardness for directed energy deposition of Ti6Al4V[J], Add. Manufact. 35 (2020) 101252.
[28] C. Baykasoglu, O. Akyildiz, D. Candemir, et al., Predicting microstructure evolution during directed energy deposition additive manufacturing of Ti-6Al-4V[J], J. Manuf. Sci. Eng. 140 (5) (2018), 051003.
[29] F. Calignano, Design optimization of supports for overhanging structures in aluminum and titanium alloys by selective laser melting[J], Mater. Des. 64 (2014) 203–213.
[30] M. Langelaar, Combined optimization of part topology, support structure layout and build orientation for additive manufacturing[J], Struct. Multidiscip. Optim. 57 (5) (2018) 1985–2004.
[31] G. Allaire, B. Bogosel, Optimizing supports for additive manufacturing[J], Struct. Multidiscip. Optim. 58 (6) (2018) 2493–2515.
[32] L. Cheng, X. Liang, J. Bai, et al., On utilizing topology optimization to design support structure to prevent residual stress induced build failure in laser powder bed metal additive manufacturing[J], Add. Manufact. 27 (2019) 290–304.
[33] N. Gardan, A. Schneider, Topological optimization of internal patterns and support in additive manufacturing[J], J. Manuf. Syst. 37 (2015) 417–425.
[34] M. Cervera, C. Agelet de Saracibar, M. Chiumenti, COMET: Coupled mechanical and thermal analysis, Data Input Manual, Version 5.0, Technical Report IT-308, 2002 http://www.cimne.com.
[35] M. Chiumenti, X. Lin, M. Cervera, et al., Numerical simulation and experimental calibration of additive manufacturing by blown powder technology. Part I: thermal analysis[J], Rapid Prototyp. J. 23 (2) (2017) 448–463.

[36] M. Chiumenti, M. Cervera, A. Salmi, et al., Finite element modeling of multi-pass welding and shaped metal deposition processes[J], Comput. Methods Appl. Mech. Eng. 199 (37–40) (2010) 2343–2359.
[37] M. Chiumenti, M. Cervera, N. Dialami, et al., Numerical modeling of the electron beam welding and its experimental validation[J], Finite Elements Analysis Design 121 (2016) 118–133.
[38] Y. Ueda, H. Murakawa, N. Ma, Welding Deformation and Residual Stress Prevention, Elsevier, 2012.
[39] Erik R. Denlinger, P. Michaleris, Effect of stress relaxation on distortion in additive manufacturing process modeling[J], Add. Manufact. 12 (2016) 51–59.
[40] T. Kawaoka, Introduction of the personal pre-post processor GiD[J], Proceed. Design Systems Conf. 12 (2002) 151–153.
[41] V. Fallah, M. Alimardani, S.F. Corbin, et al., Temporal development of melt-pool morphology and clad geometry in laser powder deposition[J], Comput. Mater. Sci. 50 (7) (2011) 2124–2134.
[42] S. Afazov, W.A.D. Denmark, B.L. Toralles, et al., Distortion prediction and compensation in selective laser melting[J], Add. Manufact. 17 (2017) 15–22.